Element sensitive holographic imaging of atomic structures using white x rays

K. M. Dąbrowski, D. T. Dul, T. P. Roszczynialski, and P. Korecki*
Institute of Physics, Jagiellonian University, Reymonta 4, 30-059 Kraków, Poland
(Received 7 December 2012; published 28 February 2013)

White-beam x-ray fluorescence holograms were recorded using a 50 watt x-ray tube for a Cu_3Au single crystal. Element sensitivity for this model sample was explicitly demonstrated by measuring distinct holograms using Cu K and Au L x-ray fluorescence. The phase sensitivity of the recorded holograms enabled us to obtain projections of the local atomic structure and image the electron density within the unit cell, relative to either Au or Cu atoms. Since the experimental setup does not require any optics and the angular resolution requirements are loose, the application of more powerful laboratory x-ray sources is straightforward.

DOI: 10.1103/PhysRevB.87.064111 PACS number(s): 61.05.C−, 42.40.−i, 78.70.En, 42.30.Rx

I. INTRODUCTION

X-ray fluorescence holography (XFH)[1] provides the means for obtaining three-dimensional (3D) images of local atomic structure. The main driving force behind its development was the desire to overcome the phase problem of standard diffraction methods. An x-ray fluorescence hologram is formed as a result of the interference of the incident radiation and x rays scattered inside the sample. Therefore, similarly to Gabor holograms,[2] x-ray fluorescence holograms contain the amplitude and the phase information of the scattered radiation. This interference is probed at the atomic sites by measuring x-ray fluorescence emitted by atoms. A 3D image around absorbing atoms can be obtained from holograms using numerical reconstruction.[3] However, because of a very weak holographic signal ($\sim 10^{-3}$ of the average fluorescence yield) and the necessity to record multiple holograms for twin-image removal,[4,5] experiments usually require intense synchrotron radiation. In the case of monochromatic XFH, only a few attempts have been made using conventional x-ray sources.[1,6–9] For a review of XFH and recent application examples, see Refs. 10 and 11.

A way around to solve the twin-image problem is to use a white beam for recording x-ray fluorescence holograms. The transition from monochromatic to polychromatic illumination is accompanied by a qualitative change of the x-ray hologram character.[12,13] Because of the short coherence length of the white beam, the interference effects are constrained around forward scattering. This effect is exemplified in Fig. 1(a), which shows spatial modulations of the total x-ray field induced by scattering of the incident polychromatic plane wave on a single atom. The main feature is the specific "shadow" in the forward direction. The drop in the intensity at the forward-scattering direction is due to the negative scattering amplitude of x rays. Figures 1(b) and 1(c) show a similar calculation for a crystal. In this case, the enhanced forward scattering results in a localization of the x-ray field minima on dense-packed atomic chains. This effect determines the main features of the hologram. Since a hologram is measured by probing the x-ray field at the atomic sites (via fluorescence yield emitted from particular elements) when the sample is rotated relative to the incident-beam direction, one can observe signal variations near directions coinciding with dense-packed directions and planes. The calculations from Fig. 1 were performed using the formalism of Ref. 14 for a spectrum characteristic of an x-ray tube operating at 50 kV, as described in the remainder of this paper.

Until now, white-beam x-ray fluorescence holograms were measured exclusively at synchrotrons. For example, in a recent experiment,[15] high-resolution projections of atomic structure around absorbing atoms were observed for a hard x-ray wiggler radiation with a mean energy above 60 keV and a spread of almost 40 keV. Initial experiments employed total electron yield for measuring the variation of the x-ray field at atomic sites. Therefore, the term *white-beam x-ray fluorescence holography* was first used in Ref. 16.

In this work, we recorded white-beam x-ray fluorescence holograms in a laboratory using a low-power 50 watt x-ray tube. Moreover, we explicitly showed element sensitivity of XFH by recording distinct holograms for Au and Cu atoms in the Cu_3Au alloy. The experiment was possible by exploiting the relative large photoelectric absorption cross section in the energy range around 20 keV (changing with $\sim 1/E^3$), which compensated for the small intensity of an ordinary x-ray tube compared to synchrotron radiation. Despite this *relatively* soft x-ray spectrum, we were able to obtain projections of local atomic structure around Au and Cu atoms and determine the electron density within the unit cell relative to those atoms.

II. EXPERIMENT

The scheme of the experimental setup for laboratory recording of white-beam x-ray fluorescence holograms is presented in Fig. 2(a). A 50 W x-ray tube (50 kV, 1 mA, 0.8 Al filter) with a tungsten anode and a spot size of 75 μm was used as a source of polychromatic x rays. A circular aperture with diameter of 8 mm at a distance of 340 mm from the x-ray tube was used to shape the beam with approximately 2×10^8 photons/s. Originally this setup was devoted to experiments with polycapillary optics.[6]

A Cu_3Au single crystal in the ordered phase with a (001) orientation was used in the experiment. The sample had a diameter of 10 mm and a thickness of 1 mm. The choice of Cu_3Au (space group $Pm\bar{3}m$, lattice constant $a = 3.75$ Å) was made, as it can be seen as a model system in x-ray holography for which computational[18] and experimental studies were performed.[19] Moreover, for x-ray holograms recorded with a monochromatic 10 keV incident beam, significant extinction effects were observed.[20]

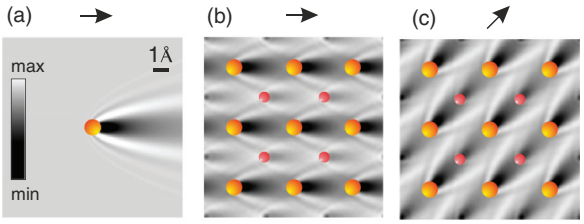

FIG. 1. (Color online) Spatial modulation of the x-ray field intensity due to the interference between incident plane wave and scattered radiation for a white-beam case. (a) Single atom. (b), (c) Crystal. Arrows denote the direction of the incident beam. A white-beam x-ray hologram is measured by probing this modulation at atomic sites (via x-ray fluorescence) while the crystal is rotated relative to the incident-beam direction. The "shadowing" effect enables one to directly observe signal variations near directions coinciding with dense-packed directions and planes and the higher-order diffraction effects enable 3D imaging.

The sample was placed at a distance of 610 mm from the source and was rotated relative to the incident beam around two axes (θ,ϕ). The data were collected on $\Delta\phi = 0.15^\circ$, $\Delta\theta = 0.5^\circ$ mesh in the θ range from 26.5° to 80° as measured from the sample's normal. For further analysis, the collected data were rebinned in the ϕ direction to a mesh compatible with the angular resolution of the setup determined by the sample's angular diameter ($<1^\circ$). For each sample orientation an x-ray fluorescence spectrum [cf. Fig. 2(b)] was recorded for 0.5 s using an energy resolving silicon drift detector (SDD) with an area of 25 mm^2, thickness of 500 μm, placed at a distance of 12 mm from the sample. The detector was attached to the θ circle and positioned along the surface normal. This experimental geometry enabled us to avoid the problem of simultaneous recording of Kossel lines, which can be observed in emission geometry.[21] The fluorescence detection rate was at the level of 10^5 photons/s. The Cu K and Au L fluorescence yields (Y_{Cu} and Y_{Au}) were computed from the spectra and subsequently corrected for dead time. The total acquisition time was ~90 h. Note that the times needed for acquisition of a full multiple-energy data set at synchrotrons are of the same order.[22]

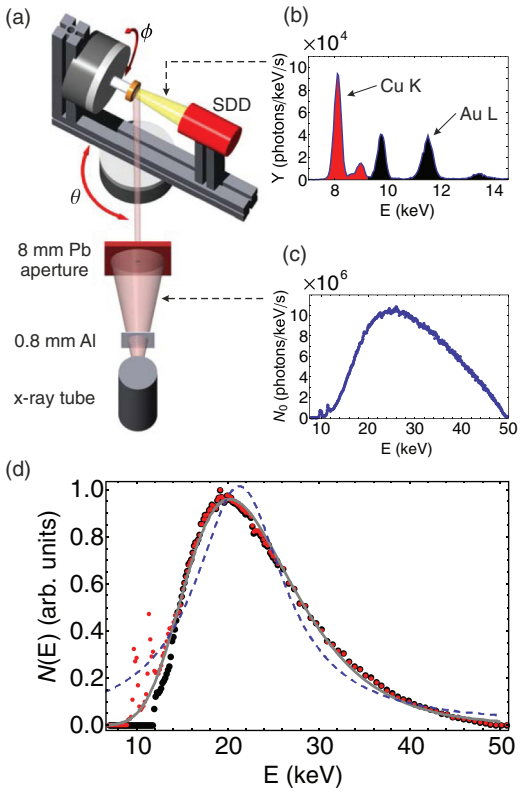

FIG. 2. (Color online) (a) Scheme of the experimental setup for laboratory recording of white-beam x-ray fluorescence holograms. (b) Spectrum of the emitted x-ray fluorescence $Y(E)$ with visible Cu K and Au L lines. (c) Spectrum of the incident beam $N_0(E)$. (d) Effective energy spectra $N(E)$. Small red circles show the spectrum for Cu atoms and large black circles show the spectrum for Au atoms. Dashed and solid lines are Lorentz ($E_0 = 21.3$ keV, $\Delta E = 11.9$ keV) and Gumbel ($\varepsilon_0 = 20.2$ keV, $\Delta\varepsilon = 5.9$ keV) fits to the data.[17]

For white-beam XFH, the main parameter influencing the character of the holograms is the so-called effective energy spectrum $N(E)$. Roughly speaking, it is a spectrum sensed by atoms inside the sample. In previous works performed for hard synchrotron radiation, a thin object approximation was used. In the present work, in order to take into account the non-negligible escape depth of the fluorescence radiation as compared to penetration depth of the incident beam, $N(E)$ has to be defined using formulas taken from x-ray spectroscopy,[23] i.e., as $N(E) = N_0(E)\eta(E)$, where $N_0(E)$ is the incident-beam spectrum, $\eta(E) = \mu_i(E)/[\mu(E)/\cos\theta + \mu(E_i)]$, $\mu_i(E)$ is the photoelectric absorption coefficient of atoms of type i, $\mu(E)$ is the total absorption coefficient of the sample, and E_i is the effective energy of x-ray fluorescence emitted by atoms of type i (Au or Cu).

The incident-beam spectrum $N_0(E)$ was measured directly with the SDD by placing it far from the source and correcting it by the energetic efficiency curve. The $N_0(E)$ spectrum is shown in Fig. 2(c). $\eta(E)$ was computed using the procedures from the XRAYLIB library.[24] The resulting effective spectra for Cu and Au atoms, averaged over the sample's orientation, are shown in Fig. 2(d). The spectra are very similar except for the low-energy part where one observes a jump corresponding to the Au L3 absorption edge in the Au spectrum and characteristic W emission lines for the Cu spectrum. The area of these lines is small, i.e., of the order of 2% of the total spectrum.

III. WHITE-BEAM X-RAY FLUORESCENCE HOLOGRAMS

White-beam x-ray fluorescence holograms recorded for Au (χ_{Au}) and Cu (χ_{Cu}) atoms are shown in Fig. 3. They were extracted from florescence yields measured as the function of the sample orientation relative to the incident-beam direction according to $\chi_i(\theta,\phi) = Y_i(\theta,\phi)/Y_i^0(\theta,\phi) - 1$, where $Y_i^0(\theta,\phi)$ is the slowly varying component of the signal. The background subtraction was performed using smoothing splines. The holograms were symmetrized using the $Pm\bar{3}m$ space group and extended to the full sphere. Areas around the $\langle 001\rangle$ directions were not accessible due to the specific mounting of the detector. For comparison, parts of the experimental data were replaced by calculated data. In the calculation, the effective energy spectrum $N(E)$ was approximated by the

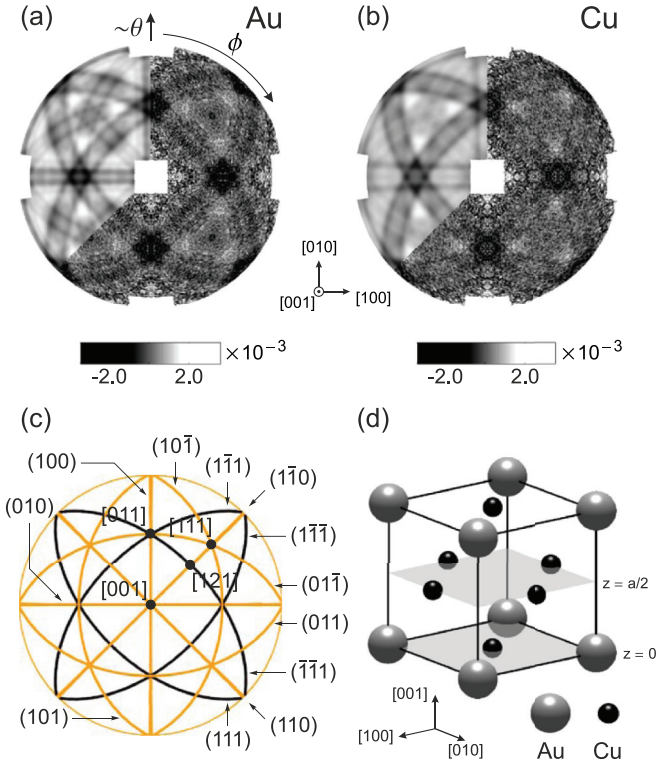

FIG. 3. (Color online) White-beam x-ray fluorescence holograms recorded for a Cu_3Au crystal. Hologram recorded for (a) Au L fluorescence and (b) Cu K fluorescence. For comparison, parts of the experimental data were replaced by calculated data. The contrast has been enhanced for better presentation. Both patterns are presented as equal-area projections of the upper part of the hemisphere. (c) Corresponding projection of dense-packed atomic planes in Cu_3Au. Lines around which the holograms are expected to significantly differ are shown in color. (d) The unit cell of Cu_3Au.

Gumbel function, which accounts for the skewness of the spectrum [cf. Fig. 2(d)]. For details of the calculations, see Ref. 16.

The most characteristic features of the recorded white-beam holograms are the bands which are centered around projections of dense-packed atomic planes. For a direct comparison, Fig. 3(c) shows a purely geometrical projection of the low-index atomic planes in the Cu_3Au sample. In addition, the data show distinct minima at the crossing of these bands which coincide with the dense-packed directions. For the Cu_3Au structure, there are essentially two kinds of atomic planes. The first type is composed of both Au and Cu atoms, while the second type contains only Cu atoms. Hence, one can expect that the holograms measured for Au or Cu fluorescence will mainly differ near the projection of these planes [cf. Fig. 3(c)]. This effect, which is clear in simulated data, can be also directly observed in the measured data.

IV. RECONSTRUCTION OF ATOMIC STRUCTURE

In order to retrieve the structural information from the measured holograms, two approaches were used: wavelet analysis[16,25] and a linear regression approach.[18] The first method is model free and allows one to obtain projections of the local atomic structure. The linear regression algorithm, which is a generalization of the tomographic approach,[14] enables 3D imaging of the unit cell but assumes periodicity and requires the knowledge of the unit-cell parameters. Moreover, these two methods rely on different features of the holograms. The wavelet transform uses the information contained around dense-packed atomic directions, while the linear regression approach uses the whole visible bands around projections of atomic planes.

A. Local structure imaging using wavelet analysis

As the wavelet analysis of white-beam x-ray holograms has been described previously,[25] here we will give only a brief description of it. The wavelet analysis takes advantage of unique properties of the holographic signal recorded for a white beam, which can be written as

$$\chi(\hat{\mathbf{k}}) = -2r_e \int_V \frac{\rho(\mathbf{r})}{r} h(\vartheta, r)\, dV, \tag{1}$$

where $\hat{\mathbf{k}}$ defines the incident-beam direction, $\mathbf{r}$ is the position relative to the absorbing atom, $\rho(\mathbf{r})$ is the electron density of the sample, r_e is the classical electron radius, V is the sample volume, and $\vartheta = \arccos(\hat{\mathbf{k}} \cdot \hat{\mathbf{r}})$. For a Lorentzian approximation of the effective spectrum,

$$h(\vartheta, r) \approx \exp(-\Delta k r \vartheta^2/4)\cos(k_0 r \vartheta^2/2), \tag{2}$$

where k_0 is the center and Δk is the FWHM of $N(k)$. Due to the short coherence length of a white beam, all $h(\vartheta, r)$ functions are localized around directions in which the scattering atoms are located. They have an almost zero mean and are similar, i.e., they differ only in scale and position on the sphere. Note that these general properties are independent of the specific shape of the x-ray spectrum unless it is sufficiently white. Since $h(\vartheta, r)$ functions closely resemble wavelets, the spherical wavelet transform[26] is a natural way for analysis of white-beam holograms. In particular, a windowed inverse wavelet transform was shown to produce high-quality spherical projections of the local atomic structure. It improves the quality of the structural images compared to a direct wavelet transform. However, this happens at the expense of resolution degradation along the radial direction.

In a recent work,[16] a compact formula was given for computing this transform:

$$F(\hat{\mathbf{k}}) = C_\psi \int_{S^2} \chi(\hat{\mathbf{k}}')\Psi(\hat{\mathbf{k}}', \hat{\mathbf{k}})\, d\Omega, \tag{3}$$

where C_ψ is a constant and

$$\Psi(\hat{\mathbf{k}}', \hat{\mathbf{k}}) = \frac{e^{-\frac{1}{4}\Delta k r_c \vartheta^2} \sin\left(\frac{k r_c \vartheta^2}{2}\right) - e^{-\frac{1}{4}\Delta k r_0 \vartheta^2} \sin\left(\frac{k r_0 \vartheta^2}{2}\right)}{k r_0 \vartheta^2}. \tag{4}$$

In this expression, $\vartheta = \arccos(\hat{\mathbf{k}}' \cdot \hat{\mathbf{k}})$. The inverse windowed wavelet transform is determined by two parameters: r_0 and r_c. In this work, r_0 was set to the smallest possible value of 2 Å, determined by specific limitations of the wavelet transform.[16] The r_c parameter was used to adjust the depth of the view of the projection, $\Delta r \sim r_c(1 + \Delta k/k_0)$. Therefore, signals from atoms located at distances larger then Δr will be strongly suppressed in the projection.

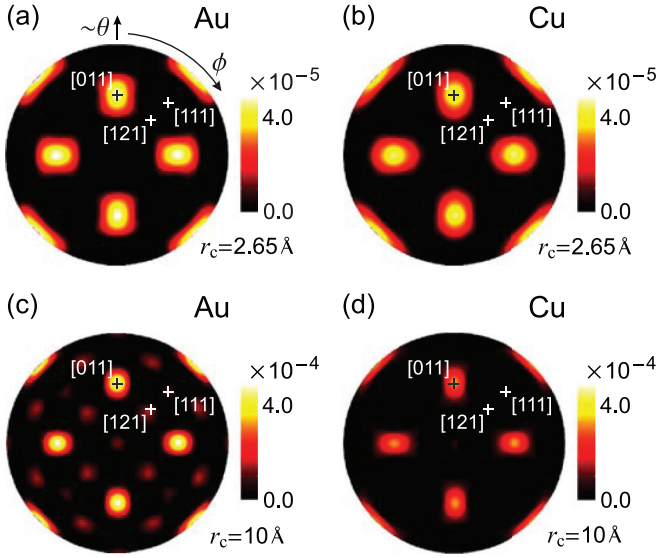

FIG. 4. (Color online) Projections of local atomic structure obtained with the inverse windowed wavelet transform of white-beam fluorescence holograms for Au and Cu absorbing atoms. Images in (a) and (b) were obtained for $r_c = 2.65$ Å and in (c) and (d) for $r_c = 10$ Å. The angular and intensity scales can be directly compared to those from Fig. 3.

Figure 4 shows projections of the atomic structure around Au and Cu atoms obtained from holograms presented in Fig. 3 by means of the windowed inverse wavelet transform. The parameters k_0 and Δk were obtained from a fit to the measured spectrum as shown in Fig. 2(d). Images were computed for $r_c = 2.65$ Å (nearest atom distance in the ⟨011⟩ direction) and for $r_c = 10$ Å. The spots visible in the images coincide with directions of dense-packed atomic rows, which means that individual atomic chains can be visualized using the wavelet analysis of white-beam holograms. For larger r_c, spots having larger interatomic spacing become visible.

Note that for the Cu_3Au sample, the positions of atoms in the local structure around Au and Cu atoms are the same. These positions are, however, occupied by different types of atoms. Hence, one can expect that the projection will differ only in intensities. For example, in the ⟨011⟩ direction, for an Au absorber, the sequence of atoms is Cu-Au-Cu. In the unit cell, there are three Cu atoms having a different position. Therefore, for an average Cu absorber, this sequence is X-Cu-X, where X corresponds to a site with occupancy $\frac{1}{3}$Au and $\frac{2}{3}$Cu. Hence, the nearest neighbor of the Cu absorber has an effectively larger scattering amplitude than the nearest neighbor of the Au absorber. On the other hand, for the Au absorber, the total number of electrons in this chain is effectively higher than for the Cu absorber. This situation is reflected in the experimental results. For $r_c = 10$ Å, the ⟨011⟩ spots in the Au data are significantly stronger compared to the Cu data. For this relatively large r_c, the total number of electrons in the chain becomes the dominant factor of the observed intensity. This also explains the very weak intensity of spots at the ⟨121⟩ and ⟨111⟩ directions for Cu data compared to Au data. However, for $r_c = 2.65$ Å, the spots at the ⟨011⟩ directions have comparable intensity in Au and Cu data. Hence, for a small value of r_c, the dominant contribution to the signal comes from the nearest atoms. This demonstrates that white-beam fluorescence holograms were recorded with sensitivity enabling one to detect atoms in the local structure which produce holographic oscillations at the level of 10^{-4} of the total signal. The angular diameters of visible spots can be directly converted to spatial resolution in the tangential plane. For example, at the [011] direction for a tangential plane at 2.65 Å, the resolution is 1.4 Å.

B. Reconstruction of electron density with linear regression

According to Refs. 14 and 27, for a periodic sample, the hologram can be described as a linear superposition of terms corresponding to different reciprocal space vectors **H**:

$$\chi(\hat{\mathbf{k}}) = -\frac{8\pi r_e}{V}\sum_{\mathbf{H}} F_{\mathbf{H}}\chi_{\mathbf{H}}(\hat{\mathbf{k}}), \tag{5}$$

where V is unit cell volume and $F_{\mathbf{H}}$ are the structure factors. A generalization to noncentrosymmetric positions is possible. Again, for a Lorentzian approximation of the effective energy spectrum, a compact form for the $\chi_{\mathbf{H}}$ functions can be obtained. In such a case,[14]

$$\chi_{\mathbf{H}}(\hat{\mathbf{k}}) = \frac{H^2 + 2k_0\mathbf{H}\cdot\hat{\mathbf{k}}}{W} + \frac{\Delta k\mathbf{H}\cdot\hat{\mathbf{k}}}{AW}\ln\left[\frac{4\kappa_+^2(\mathbf{H}\cdot\hat{\mathbf{k}})^2}{H^4}\right] \tag{6}$$

and

$$W = H^4 + 4k_0H^2\mathbf{H}\cdot\hat{\mathbf{k}} + 4\kappa_+^2(\mathbf{H}\cdot\hat{\mathbf{k}})^2, \tag{7}$$

where $A = \pi + 2\arctan(2k_0/\Delta k)$ and $\kappa_+ = \sqrt{k_0^2 + (\Delta k/2)^2}$. A single intensity band visible in the experimental data corresponds to the set of all colinear reciprocal vectors **H**.

In Ref. 14, a quantitative tomographic algorithm was proposed for imaging of 3D structure from white-beam holograms. This algorithm, which explicitly takes advantage of the projectionlike character of white-beam x-ray holograms, is based on measuring of the signal amplitude at the center of bands where the projection interpretation is straightforward. In this work, because of the small number of observed bands, a direct application of the tomographic algorithm resulted in low-resolution images. On the other hand, the softer energy spectrum allowed us to resolve individual $\chi_{\mathbf{H}}$ in a single band (which was not possible in previous synchrotron experiments). Therefore, the structure factors $F_{\mathbf{H}}$ can be obtained by a linear regression procedure.[18] Since both the value and sign of $F_{\mathbf{H}}$ can be extracted, one is able to reconstruct the sample electron density by a simple Fourier sum:

$$\rho(\mathbf{r}) = \frac{1}{V}\sum_{\mathbf{H}} F_{\mathbf{H}}e^{i\mathbf{H}\cdot\mathbf{r}}. \tag{8}$$

In the reconstruction procedure, 32 basis functions in four reciprocal space shells were fitted to the experimental data. The results of the fitting procedure are shown in Figs. 5(a) and 5(b). The reconstructed holograms calculated by means of Eq. (5) and the determined structure factors well describe the experimental holograms from Figs. 3(a) and 3(b).

The retrieved structure factors $F_{\mathbf{H}}$ were then used to determine the electron density, which is visualized in Figs. 5(c)–5(f). The isosurface plots are shown for two different values of

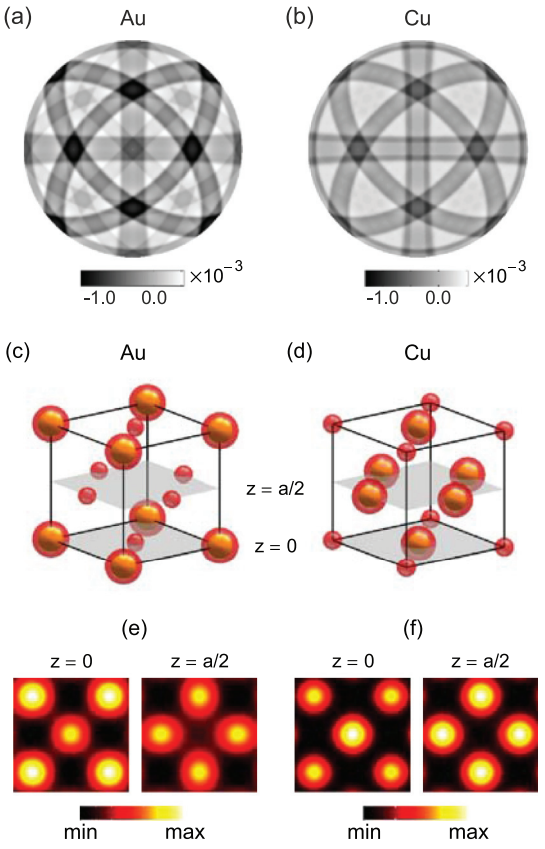

FIG. 5. (Color online) Reconstruction of the electron density for recorded Au and Cu holograms. Fitted $\chi_{\mathbf{H}}$ basis functions for (a) Au and (b) Cu data. (c), (d) 3D isosurface plots of the reconstructed electron density. (e), (f) The reconstructed electron density at $z = 0$ and $z = a/2$ [cf. Fig. 3(d)] for Au and Cu, respectively.

the reconstructed electron density. For a better visualization, two-dimensional cross sections at $z = 0$ and $z = a/2$ are shown.

The analysis of the Au data is straightforward. The reconstruction shows the electron density $\rho(\mathbf{r})$ inside the unit cell relative to the position of the Au atom. The visible strong maxima at the corners correspond to Au atoms, and the weaker ones, located at the faces of the unit cell, correspond to Cu atoms. For Cu data, the interpretation is a bit more complex since there are three nonequivalent positions of Cu atoms inside the cell. Therefore, data show ρ relative to the Cu atoms and averaged over the three positions. Consequently, the corners of the visualized unit cells correspond to sites occupied with Cu atoms, while the faces correspond to sites with an occupancy of $\frac{2}{3}$Cu and $\frac{1}{3}$Au. The nominal (noise-limited) resolution of the data is 1.7 Å.[28] However, the precision of atomic position determination is an order of magnitude better.

There is a small discrepancy between the reconstructed and expected electron densities. In fact, similar differences are present in the results obtained by means of the wavelet analysis. This is partially due to parasitic effects of secondary fluorescence and total absorption. In the future, these effects can be corrected using numerical methods of x-ray fluorescence spectroscopy.[23] In addition, the wavelet and linear regression analysis can be further improved by using more exact approximations of the effective spectra.

V. CONCLUSION

When a white x-ray beam illuminates a crystal, the diffracted beams give rise to a Laue pattern, as discovered 100 years ago. Nowadays, the Laue method is most frequently used for sample orientation. It analyzes all of the allowed diffraction beams, except the forward-scattered one (zeroth-order diffraction). In this work, we showed that by using a low-power x-ray tube and by probing the interference of a forward-scattered white beam inside the sample, one is able to obtain phase-sensitive information about the structure and also obtain element selectivity via fluorescence detection. On the one hand, the recording of white-beam x-ray fluorescence holograms in a laboratory could be treated just as a curiosity. On the other hand, in the used experimental geometry, the angular resolution is mainly limited by the sample size. Therefore, the use of x-ray sources with larger spots would not result in resolution deterioration. In addition, the presented experiment was performed without any x-ray optics needed for collimation or monochromatization. This means that a standard 60 kV x-ray tube with spot size of 1 mm and power of 3 kW could be used in experiments. This denotes almost 100 times more photons on the sample. By using rotating anode x-ray tubes, the gain in the photon flux could even be much larger. These numbers indicate the possibilities of real structural studies in samples containing 1% of foreign atoms or in thin films or multilayers.

ACKNOWLEDGMENTS

This work was supported by the Polish National Science Center (Grant No. DEC-2011/01/B/ST3/00506). K.M.D. and D.T.D. acknowledge support from the Jagiellonian University's DSC program (Grant No. DSC/000692/2012).

*pawel.korecki@uj.edu.pl

[1] M. Tegze and G. Faigel, Nature (London) **380**, 49 (1996).
[2] D. Gabor, Nature (London) **161**, 777 (1948).
[3] J. J. Barton, Phys. Rev. Lett. **61**, 1356 (1988).
[4] J. J. Barton, Phys. Rev. Lett. **67**, 3106 (1991).
[5] T. Gog, P. M. Len, G. Materlik, D. Bahr, C. S. Fadley, and C. Sanchez-Hanke, Phys. Rev. Lett. **76**, 3132 (1996).
[6] K. M. Dąbrowski and P. Korecki, Nucl. Instrum. Methods Phys. Res., Sect. B **285**, 94 (2012).
[7] Y. Takahashi, K. Hayashi, and E. Matsubara, Powder Diffr. **19**, 77 (2004).
[8] M. Tegze, G. Faigel, S. Marchesini, M. Belakhovsky, and A. I. Chumakov, Phys. Rev. Lett. **82**, 4847 (1999).
[9] S. G. Bompadre, T. W. Petersen, and L. B. Sorensen, Phys. Rev. Lett. **83**, 2741 (1999).
[10] K. Hayashi, N. Happo, S. Hosokawa, W. Hu, and T. Matsushita, J. Phys.: Condens. Matter **24**, 093201 (2012).

[11]G. Faigel, G. Bortel, C. S. Fadley, A. S. Simionovici, and M. Tegze, X-Ray Spectrom. **36**, 3 (2007).
[12]P. Korecki and G. Materlik, Phys. Rev. Lett. **86**, 2333 (2001).
[13]P. Korecki, M. Tolkiehn, and D. Novikov, Radiat. Phys. Chem. **78**, S34 (2009).
[14]P. Korecki, M. Tolkiehn, D. V. Novikov, G. Materlik, and M. Szymoński, Phys. Rev. B **74**, 184116 (2006).
[15]P. Korecki, M. Tolkiehn, K. M. Dąbrowski, and D. V. Novikov, J. Synchrotron Radiat. **18**, 851 (2011).
[16]D. T. Dul and P. Korecki, New J. Phys. **14**, 113044 (2012).
[17]The Lorentz function is defined as $N_L(E) = (A/2\pi)\frac{\Delta E}{(E-E_0)^2+(\Delta E/2)^2}$, where E_0 is its mean and ΔE is the FWHM. The Gumbel function is defined as $N_G(E) = (A/\Delta\varepsilon)\exp[-\exp(-(E-\varepsilon_0)/\Delta\varepsilon) - (E-\varepsilon_0)/\Delta\varepsilon]$, where ε_0 is its mode and $\Delta\varepsilon$ determines the spread being $\sim 2.57\Delta\varepsilon$. In both functions, A is the height constant.
[18]F. N. Chukhovskii and A. M. Poliakov, Acta Crystallogr. Sect. A **59**, 109 (2003).
[19]B. Adams, D. V. Novikov, T. Hiort, G. Materlik, and E. Kossel, Phys. Rev. B **57**, 7526 (1998).
[20]P. Korecki, D. V. Novikov, M. Tolkiehn, and G. Materlik, Phys. Rev. B **69**, 184103 (2004).
[21]M. Markó, G. Krexner, J. Schefer, A. Szakál, and L. Cser, New J. Phys. **12**, 063036 (2010).
[22]S. Hosokawa, N. Happo, and K. Hayashi, Phys. Rev. B **80**, 134123 (2009).
[23]B. Beckhoff, B. Kanngießer, N. Langhoff, R. Wedell, and H. Wolff, *Handbook of Practical X-Ray Fluorescence Analysis* (Springer, Berlin, 2006).
[24]T. Schoonjans, A. Brunetti, B. Golosio, M. S. del Rio, V. A. Solé, C. Ferrero, and L. Vincze, Spectrochim. Acta, Part B **66**, 776 (2011).
[25]P. Korecki, D. V. Novikov, and M. Tolkiehn, Phys. Rev. B **80**, 014119 (2009).
[26]J.-P. Antoine, L. Demanet, L. Jacques, and P. Vandergheynst, Appl. Comput. Harmon. Anal. **13**, 177 (2002).
[27]P. Korecki, M. Tolkiehn, D. V. Novikov, G. Materlik, and M. Szymoński, Phys. Rev. Lett. **96**, 035502 (2006).
[28]R. E. Stenkamp and L. H. Jensen, Acta Crystallogr. Sect. A **40**, 251 (1984).